

## Temperature and Water Vapor Variability Within and Above the PBL from the Earth Remote Sensing Program of Record

Loveless M.\* , Knuteson, R., Loveless D., Pare, M., Pierce, B., Gero, J., Wagner, T., Taylor J., Garcia R., Tobin D.  
University of Wisconsin-Madison SSEC/CIMSS

### 1. INTRODUCTION

The National Aeronautics and Space Administration (NASA) Decadal Survey Incubation (DSI) is a new program element that was recommended in the 2017 Earth Science Decadal Survey and intended to accelerate readiness of high-priority observables needing science requirements refinement, technology development, and/or other advancements prior to cost-effective flight implementation in space. One of the targeted observables is the Planetary Boundary Layer (PBL). A PBL study team summarized key findings of a survey of past and current ground, aircraft, and space-based measurements (Teixeira et al., 2021). The PBL Study Report includes a Science and Applications Traceability Matrix (SATM) that highlights the four PBL science goals as well as specific science questions, geophysical variables and measurement requirements, and potential observing technologies to address these requirements. The SATM leads to the following measurement requirements (that can only be satisfied with a combination of different technologies): vertical resolutions as fine as 100-200 m, horizontal resolutions as fine as 1 km, temporal sampling of at least 4 times per day.

This abstract describes work done under a proposal funded at the UW-Madison Space Science and Engineering Center (SSEC) under NASA ROSES-2021 titled, “*Refining Planetary Boundary Layer Remote Sensing Requirements Using Merged Orbital and Sub-Orbital and Merged Active and Passive Observations From The Program Of Record (POR)*”, R. Knuteson (PI). The aim of this proposal was to exploit the current POR to address the PBL science goals through the analysis of merged datasets collocated with truth profiles for important climate regimes.

In practical terms, the analysis of these merged datasets provides the following things 1) quantification of the benefits of using a combination of instruments over two instruments alone (e.g., information content, accuracy of retrieved variables, vertical resolution) and 2) a characterization of the horizontal and vertical scales of variability within and above the PBL. This work will be used to inform sensor requirements for the future.

Under this NASA funded project, one synergistic combination studied is between the hyperspectral infrared and the differential

absorption lidar (DIAL) as described in the AMS extended abstract of Loveless, D.M. et al. (2024). This extended abstract adds the spatial and temporal variability analysis of the PBL using a combination of radio occultation (RO) and infrared (IR) sounding retrievals.

### 2. DATA

The Aqua AIRS Version 7 Level 2 (AIRS-Only) Support Product temperature and water vapor retrievals are used in this analysis (AIRS project, 2019). This product can be obtained from the NASA Goddard Earth Sciences Data and Information Services Center after creating a user profile (<https://disc.gsfc.nasa.gov/>). The AIRS Level 2 quality flag named “PBest” was applied.

COSMIC and COSMIC-2 radio occultation profile data (UCAR COSMIC Program, 2022; UCAR COSMIC Program, 2019) is obtained from the University Corporation for Atmospheric Research (UCAR) at <https://www.cosmic.ucar.edu/>. A user profile needs to be created to access the data. The COSMIC ‘climate-processed’ and ‘post-processed’ mission data are used, while the COSMIC-2 ‘near-real-time’ (nrt) data are used. Both the COSMIC and COSMIC-2 ‘wet profile’ (wetPrf) products are used for comparison to AIRS. The included quality flag ‘bad’ was used for quality control.

**Table1. Time periods analyzed for AIRS IR sounder matched with COSMIC datasets.**

	Time Period Analyzed
<b>AIRS v7 / UCAR COSMIC</b>	Jan-01-2007 – April-01-2015** **after April 2015 matchup numbers drastically reduced
<b>AIRS v7 / UCAR COSMIC-2</b>	Oct-01-2019 - Present

COSMIC data from the ROMSAF online archive (<https://rom-saf.eumetsat.int/index.php>) is also used, specifically for the RO and hyperspectral infrared synergy simulation. The data (ROMSAF, 2019) have a product ID of GRM-30-R1 and the following doi: 10.15770/EUM\_SAF\_GRM\_0003. The profile data ‘dis’ files are used, which combine contents of the ‘atm’ and ‘wet’ profile.

Data from the Atmospheric Radiation Measurement (ARM) program is used as well, specifically the radiosonde dataset named ‘sondewnpn’ and the Atmospheric Emitted

Radiance Interferometer (AERI) (Knuteson et al., 2004a, 2004b) summary data files named 'aerisummary'. Analysis was done on all fixed and mobile site data available, but this abstract shows results only from the fixed sites, focusing on the Southern Great Plains (SGP) facility (ARM user facility, 2001; ARM user facility, 2004), Northern Slope of Alaska (NSA), and Eastern Northern Atlantic (ENA). UW-Madison developed the AERI (Knuteson et al., 2004a, 2004b) for the Department of Energy (DOE) ARM program with DOE funding in the 1990's. Since that time AERI instruments have been operating at ARM fixed and mobile facilities providing continuous ground-based profiling of the PBL to complement the routine launches of Vaisala radiosondes (between 1 and 8 per day). Data from the ARM field sites are used to assess the performance of the space and aircraft-based retrievals and to help characterize the variability of the PBL temperature and water vapor.

### 3. OBJECTIVE 1: QUANTIFICATION OF THE BENEFITS OF MERGED DATASETS

In this section, three different examples of the benefits of merged datasets are illustrated: i) space-based hyperspectral IR with RO, ii) ground-based and space-based hyperspectral IR, and iii) airborne hyperspectral IR with airborne water vapor differential absorption Lidar (DIAL).

The first synergy example included here is a single profile retrieval simulation using a combination of a passive AIRS infrared satellite-based profile and an active satellite-based COSMIC radio occultation profile. The temperature and water vapor profiles are shown in Figure 1. These measurements may be combined using the optimal estimation framework. For this example, we will focus on retrieval uncertainties to quantify the improvements of this synergy. Following Rodgers (2000) the averaging kernel  $\mathbf{A}$  can be defined as:

$$\mathbf{A} = \mathbf{S} (\mathbf{K}^T \mathbf{S}_e^{-1} \mathbf{K}) \quad (1)$$

where  $\mathbf{S}_e$  is the model and measurement error covariance matrix,  $\mathbf{K}$  is the Jacobian (change in measurement with change in state vector) and  $\mathbf{S}$  is the posterior error covariance matrix defined as:

$$\mathbf{S} = (\mathbf{K}^T \mathbf{K}^T \mathbf{S}_e^{-1} \mathbf{S}_e^{-1} \mathbf{K} + \mathbf{S}_a^{-1} \mathbf{S}_a - 1)^{-1}. \quad (2)$$

$\mathbf{S}_a$  is the a priori covariance matrix, which in this case is calculated from a 10 year climatology of SGP radiosondes. For simplicity, since it is difficult to quantify model error,  $\mathbf{S}_e$  is estimated to be the instrument noise for AIRS (Pagano et al. 2014). We simulate AIRS Jacobians using a case study RO profile from ROMSAF. To bring the RO measurements into the calculation of  $\mathbf{A}$ ,  $\mathbf{S}_e$  is defined to be the ROMSAF derived profile

uncertainty for  $T$  and  $q$ .  $\mathbf{K}$  is a number of measurements by number of elements in the state vector sized matrix, with ones corresponding to which measurement aligns with each respective state vector element, and zeros elsewhere. The result shown here assumes the RO estimates at each level as independent observations, which is not necessarily true.

Given the simplified approach of integrating the RO observations into the calculation of  $\mathbf{A}$ , we focus on the uncertainty profiles derived from  $\mathbf{S}$ . The 1-sigma uncertainty profiles are the square root of the diagonal elements of  $\mathbf{S}$ . Quantities like vertical resolution and degrees of freedom (which can be calculated from  $\mathbf{A}$ ) would over-represent the value of the RO measurements given the construction of  $\mathbf{K}$  and  $\mathbf{S}_e$  for the RO measurements. The primary results, shown in Figure 2, are:

- 1) Simulated AIRS temperature uncertainties are high at the surface due to the inclusion of skin temperature in the state vector.
- 2) The synergy of AIRS+RO results in significant improvements to uncertainties in both  $T$  and  $q$ .
- 3) The synergy meets the objectives of the 2017 Decadal Survey for  $T$  and  $q$  uncertainties (1 K and 1 g kg<sup>-1</sup>).

In addition to re-assessing the construction of  $\mathbf{K}$  for the RO profile, future work needs to assess how the large horizontal averaging of the RO path can affect the uncertainty in ways that we are not currently accounting for.

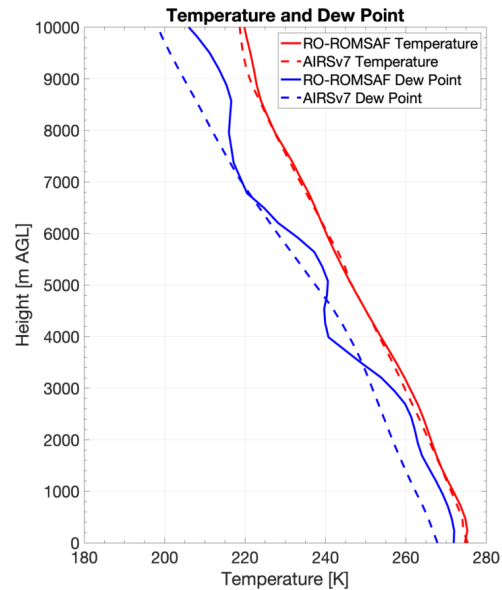
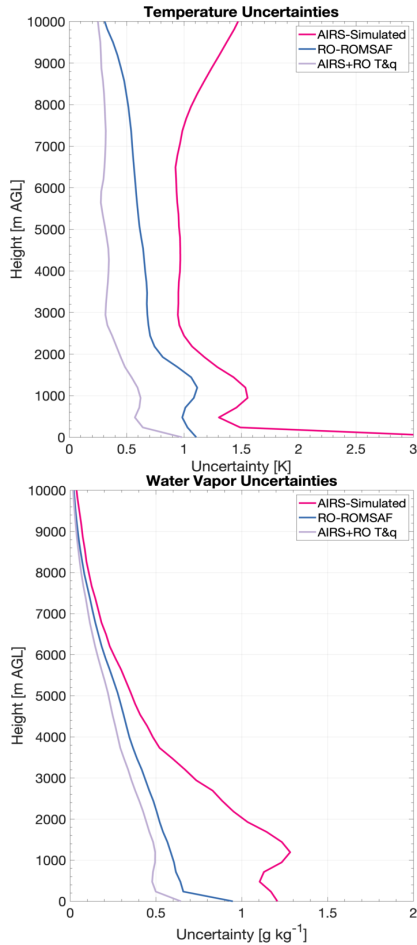


Figure 1. AIRS Version 7 and ROMSAF COSMIC temperature and dew point profile used in the passive satellite-based IR and active satellite-based RO synergy analysis example.



**Figure 2. Results of the passive satellite-based IR and active satellite-based RO synergy analysis example. Top panel shows the temperature retrieval uncertainties and bottom shows the water vapor retrieval uncertainties.**

The second synergy example shown in Figure 3 is of a passive infrared (IR) satellite-based plus passive IR ground-based measurement using the satellite-based Cross-Track Infrared Sounder and ground-based AERI. This figure is taken from Loveless et al. (2022) and shows the information in temperature gained by using a synergy of these two measurements together. Additional details about this analysis can be found in Loveless et al. (2022). A reduction in the uncertainty of the combined CrIS+AERI retrieval is seen in comparison to the individual CrIS or AERI uncertainties, especially around 1500 m. An improvement of the vertical resolution is also seen in the combined retrieval, with benefits extending from below 1000 m up to 8000 m. Uncertainties and vertical resolution of this ground-based and space-based synergy meet the objectives of the 2017 Decadal Survey in the lowest 1000 m.

The final synergy example quantifies the benefits of using the combination of an airborne

and airborne passive instrument, specifically the passive hyperspectral Scanning High-Resolution Interferometer Sounder (S-HIS) (Tobin et al., 2006) and Differential Absorption Lidar (DIAL) (Browell et al., 1998; Hair et al., 2008, Carroll et al. 2022). For simplicity in simulating the DIAL at the ARM SGP site, we utilize a water vapor retrieval uncertainty of 10% of the ambient water vapor at each level. Figure 4 shows when the S-HIS radiance measurements are combined with the water vapor measurements from the DIAL, a  $\sim 0.3$  K reduction in the temperature retrieval uncertainty is seen from  $\sim 500$  m to 7000 m. This result has been also shown from a ground-based/upward-looking perspective in Turner and Löhnert (2021). An improvement in the vertical resolution is seen as well, with the biggest gains occurring from 3000 - 9000 m, though improvements are seen above this range and below all the way to the surface.

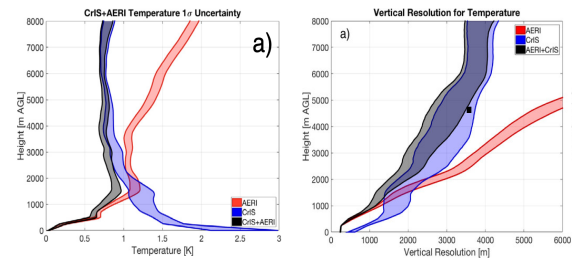


**Figure 3. Example of the passive IR satellite-based plus passive IR ground-based dataset merging: the hyperspectral infrared CrIS + AERI. Figure is taken from Loveless et al. (2022) and shows the temperature information gained by using a combination of the two datasets. (See Figure 7 and Figure 8 of Loveless et al. (2022).)**

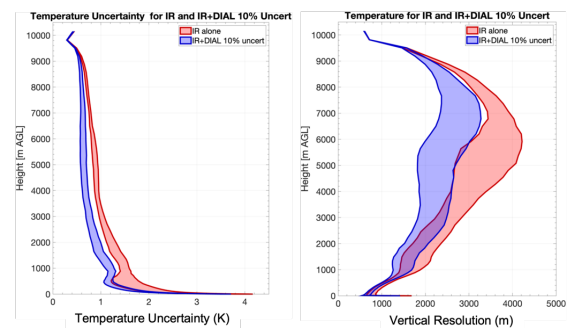


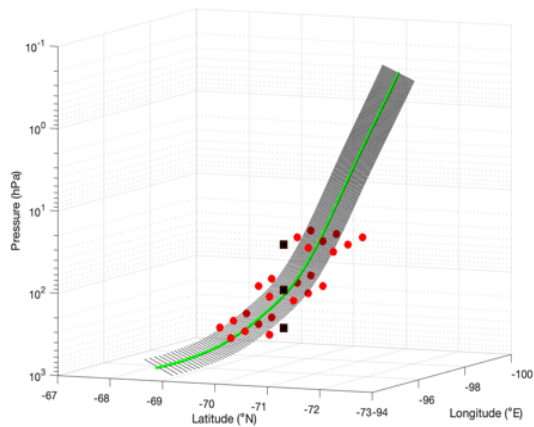
**Figure 4. Example of the passive plus active merged dataset synergy using the airborne, passive hyperspectral Scanning High-Resolution Interferometer Sounder (S-HIS) (Tobin et al., 2006) and Differential Absorption Lidar (DIAL) lidar. Figure shows the expected temperature information gained by using a combination of the two datasets for profiles from the DOE ARM SGP site in Apr-Jul 2019.**

#### 4. OBJECTIVE 2: CHARACTERIZATION OF SPATIAL AND TEMPORAL VARIABILITY WITHIN THE PBL

This section is split into two main result sections. The first result section (Section 4.1) uses a combination of passive IR sounder data and active RO data which are spatially and temporally coincident. This analysis is used to assess the IR sounder horizontal variability along the broad RO raypath and the RO vertical variability along the coarser resolution IR slant path. This variability is both the source of uncertainty in current POR retrievals and the potential source of information for future NASA sensors. The second result section (Section 4.2) uses the ground-based AERI observations to assess the temporal variability of temperature and water vapor within the PBL.

##### 4.1 RO and IR Spatial Variability

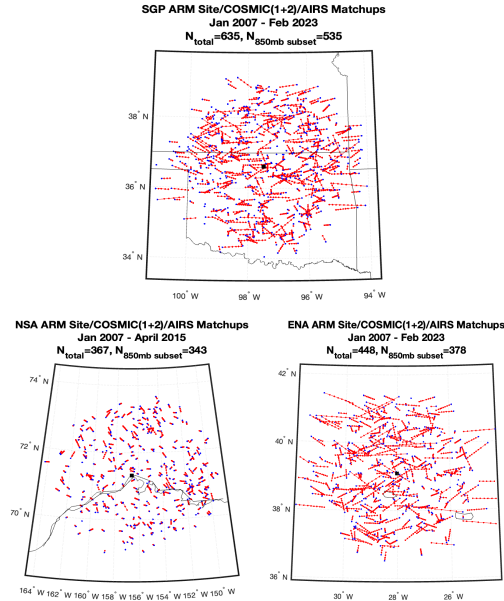
AIRS Version 7 Level 2 IR sounder data is matched with UCAR COSMIC & COSMIC-2 profiles over the approximate mission durations listed in Table 1. The raypath averaging technique as described in Feltz et al. (2014) is used where the IR sounder fields of view located along the RO profile are averaged together. This method is illustrated in Figure 5 for a single example profile matchup. A one hour time difference criterion is applied to the RO profile start time and IR measurement time.



**Figure 5. Example Aqua AIRS and COSMIC RO matchup from January 2007: A 3-D profile of the unique geometry of the RO profile (green dots & black lines) with the matching IR sounder FOVs used in the raypath averaging (red dots for 3 example pressure levels).**

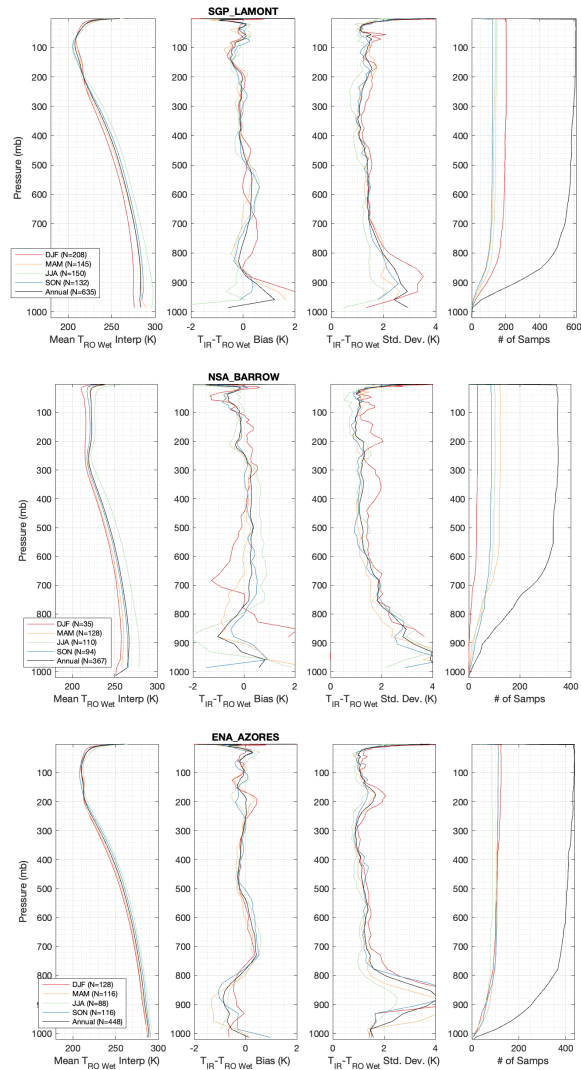
Coincident AIRS and COSMIC/COSMIC-2 profiles (which cover the globe for COSMIC/mid-latitudes for COSMIC-2) were then subset to regions centered on ARM sites (<https://www.arm.gov/capabilities/observatories/>) which are located across various climate types.

Figure 6 shows a map of the coincident AIRS and COSMIC profiles located within a 250 km radius circle centered at each of the 3 permanent ARM sites: Southern Great Plains (SGP), North Slope of Alaska (NSA), and Eastern North Atlantic (ENA.). Analysis was performed for all fixed and mobile ARM sites (25+), but the fixed sites serve as a good sample of different climate types and are shown here.



**Figure 6. Map of the COSMIC (1+2) / AIRS matchup profiles selected for analysis over the ARM Southern Great Plains (top), North Slope of Alaska (bottom left), and Eastern North Atlantic site (bottom right). The portion of the RO profile which penetrates below the 850 mb level are plotted as red lines, the blue dots indicate the closest-to-surface level of the RO profile, and the ARM site location is marked by a black marker.**

A 3-D spatial variability analysis was then performed on the subset of COSMIC and AIRS matchup profiles centered around the ARM sites, e.g. as depicted in Figure 6, for both temperature and water vapor. For reference, bias results for temperature and water vapor are shown in Figure 7 and 8 respectively for the 4 different seasons and annual average. Around 600 samples are included for the SGP site, 350 for NSA, and 400 for the ENA site, with the number of samples decreasing with lower heights. Note the height at which samples start to decrease depends on the site/atmospheric characteristics. An AIRS quality flag is used to accept vertical profiles from the top of the atmosphere down to the lowest valid retrieval level. The sensitivity of the IR to clouds leads to fewer valid matchups in the PBL.



**Figure 7. AIRS minus COSMIC RO temperature difference statistics for the SGP, NSA, and ENA ARM sites over the full coincident COSMIC 1+2 and AIRS records. Mean COSMIC temperature in Kelvin (left), bias of AIRS-COSMIC (2nd from left), standard deviation of AIRS-COSMIC (2nd from right), and number of coincident profile samples (right).**

From the bias and standard deviation errors shown in Figures 7 and 8 a few conclusions can be drawn. First the temperature bias between AIRS retrievals and COSMIC wet profiles is generally less than 1 K with the largest seasonal bias errors at the ARM NSA Barrow site. For each site the temperature standard deviation error increases substantially within or just above the PBL. The ENA Azores site in particular is a subsidence region with a common temperature capping inversion that is not captured by the IR sounding. Not surprisingly, water vapor profile errors are also largest in PBL for sites where water amounts are highest. Some of the standard

deviation error in water vapor when comparing IR to RO can be due to the horizontal averaging inherent in the radio occultation profile.

Next, Figures 9 and 10 show the horizontal spatial variability analyses for temperature and water vapor, respectively. The first columns on the left show the standard deviation of the IR sounder fields of view (FOV) that are located within the RO raypath average, and the second columns from the left show the number of FOVs used to compute that standard deviation (i.e., which are located within the RO raypath). The third columns from the left show the standard deviation of the RO levels within the AIRS IR sounder retrieval levels and the right-most columns show the associated number of samples.

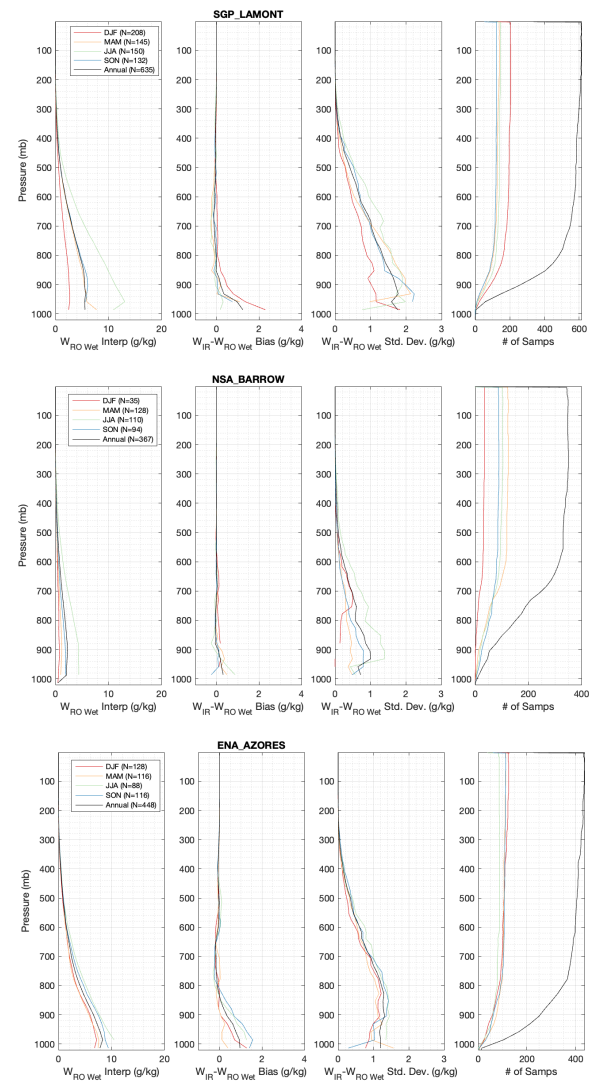


**Figure 8. Same as Figure 7 except for water vapor (g/kg).**

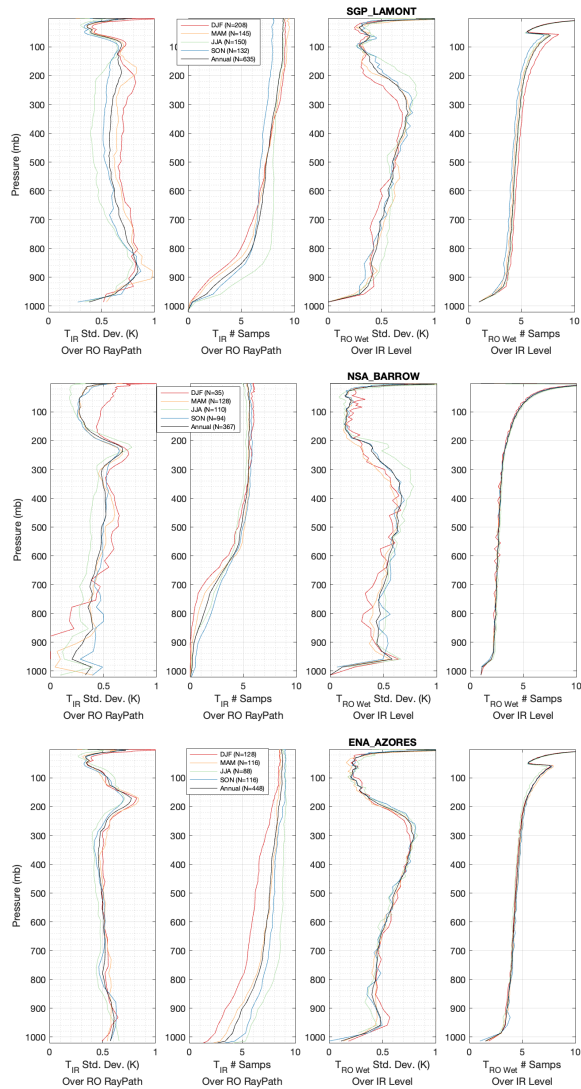


**Figure 9. AIRS and COSMIC RO Temperature spatial variability analysis for the SGP, NSA, and ENA ARM sites. The standard deviation of the IR fields of view (FOVs) over the horizontally averaged RO raypath (left) and the number of FOVs within the raypath (2nd from left). The standard deviation of the RO levels located within the AIRS 100 layers (2nd from right) and the number of RO levels within the layer (right).**

We first note that the ENA Azores ARM site has the smallest horizontal variability in temperature throughout the vertical profile with a value close to 0.5 K for all four seasons. This value of 0.5 K is the total variability which contains both the natural variability of the atmosphere and the measurement noise of the AIRS retrieval. Recent assessment of the AIRS retrieval suggests that the random noise on the AIRS temperature retrieval is about 0.3 K for clear scenes. The AIRS

profile random error increases when the scene is partially cloudy due to the cloud-clearing methodology used by the AIRS science team (Susskind et al. 1998). In contrast to the ENA Azores site, the SGP site shows significantly larger horizontal variability in the lower troposphere (altitudes below 700 hPa) and larger seasonal dependence. This behavior is expected since SGP site is a mid-latitude mid-continental site and the ENA site is dominated by sub-tropical oceans. This gives us some confidence that this methodology is providing useful characterization of the horizontal variability of temperature. The Arctic NSA site however suffers from a lack of samples in the lower atmosphere due to quality rejection of the IR profile levels, probably due to persistent cloudiness at that site.

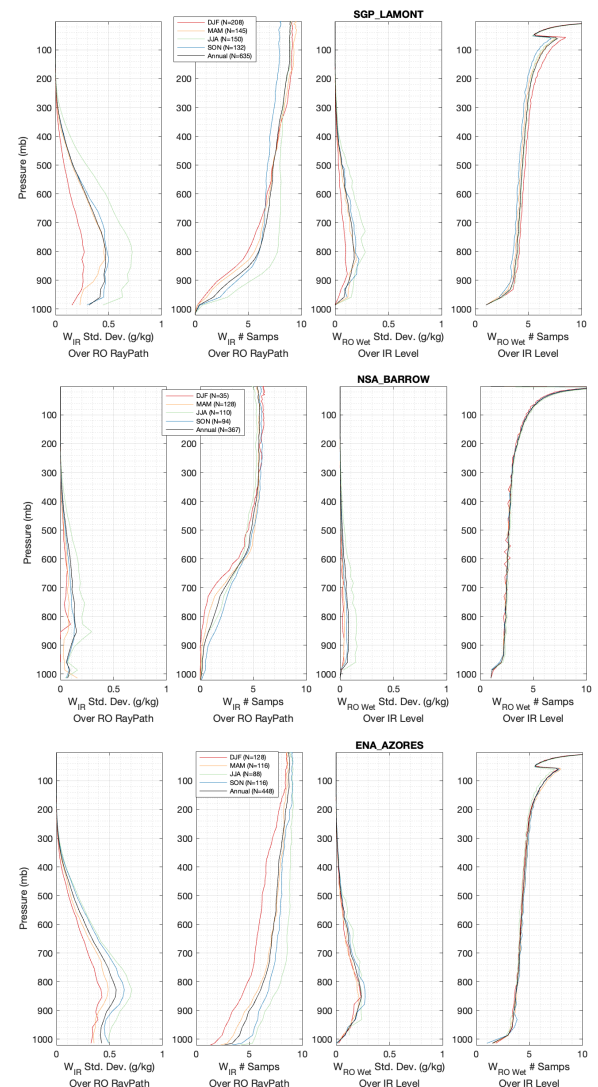
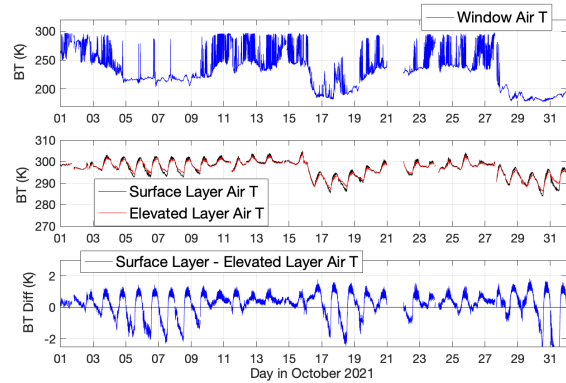


**Figure 10. Same as Figure 9 except for water vapor.**

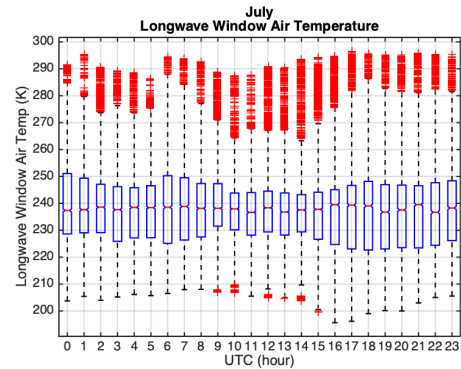
For the water vapor analysis in Figure 9, the horizontal variability is a function of the water vapor amount. This is clearly seen in the SGP site where there is a seasonal dependence of the horizontal water vapor variability. At the Azores ENA site we find that unlike the small horizontal variability of temperature, the water vapor has large horizontal variability. Note that we are characterizing the horizontal variability over the RO averaging length of about 300 km, with an AIRS sounding product footprint of about 50 km. Higher spatial resolution IR products (~15km) are available and will be included in a future analysis. The vertical variations shown in Figure 9 are fairly consistent among the ARM sites and show an increase of variability within the AIRS levels with altitude. This interesting result requires more investigation since the difference standard deviation includes error from both IR and RO sources.

#### 4.2 AERI Temporal Variability

The ground based (upward looking) AERI is used here to characterize the temporal variability of the PBL temperatures. Example timeseries of the AERI 'summary channel file' contents are shown in Figure 11 for the month of October 2021 from the ARM mobile site in Houston, Texas. The timeseries shows the longwave band variables of window air temperature (defined by the 985-990 wavenumber brightness temperatures (BTs)), surface layer air temperature (defined by the 675-680 wavenumber BTs), and the elevated layer air temperature (defined by the 700-705 wavenumber BTs). The window air temperature can be roughly used to determine cloud coverage and will show the cloud base temperature when clouds are present, and the upper air temperatures at other times. The surface and elevated layer air temperatures take advantage of the carbon dioxide absorption region of the IR spectrum and show the surface layer air temperature (~15 m height) and the temperature of an elevated layer sensitive to temperature inversions (~3 km). Thus, the difference of these two air temperatures (example shown in Figure 11's bottom panel) can be an indicator of a near surface temperature inversion. The surface layer, elevated layer and the difference of the two layer temperatures all have diurnal variations which are stronger at certain times and weaker or not present at other times. These variations are also dependent on time of year and location. A positive value of the lower panel of Figure 11 indicates a positive lapse rate where the air temperature increases approaching the surface from above. A negative value indicates the air temperature near the surface is cooler than the air above it in the PBL. The AERI is particularly well suited for measuring the thermodynamic diurnal cycle.



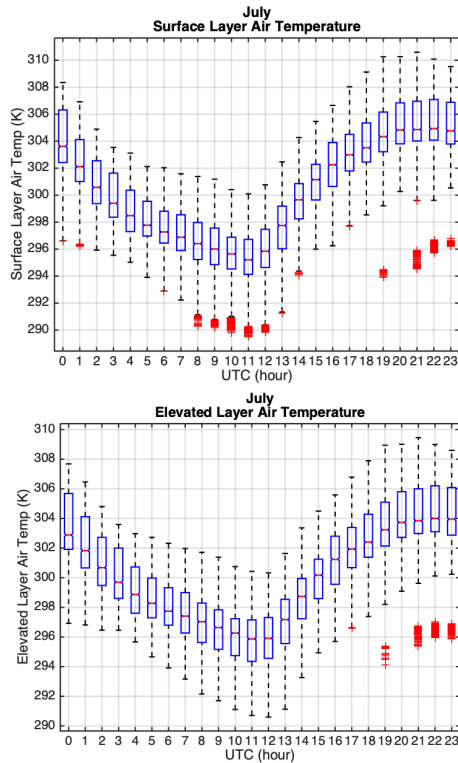
**Figure 11. AERI downwelling brightness temperature time series in Kelvin from the Houston, Texas ARM mobile campaign. (top panel) Longwave window air temperature, (middle panel) elevated layer and surface layer air temperature, and (bottom panel) the surface minus elevated layer air temperature difference.**



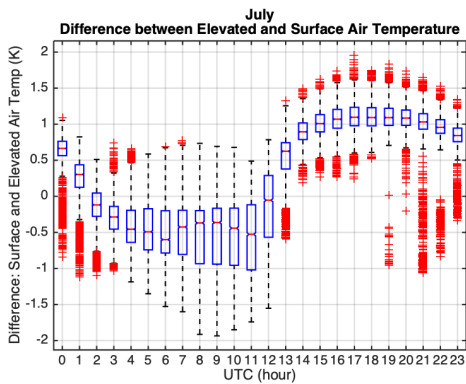
**Figure 12. July 2019 Southern Great Plains (SGP) AERI uplooking (downwelling) BT from 985-990  $\text{cm}^{-1}$  (window air T) shown in a boxplot analysis for each hour of the day (UTC hour). Central mark is the median value, the edges of the box are the 25th and 75th percentiles, the whiskers extend to the most extreme datapoints, and the outliers are plotted individually.**

Figure 12 through Figure 14 show hourly boxplots of the ARM Southern Great Plains AERI temperatures for the month of July 2019. Figure 12 shows the window air temperature and highlights the relatively warm cloud base that is present in the month of July. Figure 13 shows both the elevated and surface layer results. Note that the local sunset is around 2 UTC and local sunrise is around 12 UTC. A strong diurnal variation in temperature is present in both layer temperatures. Lastly Figure 14 shows the difference of the surface and elevated layer and highlights the strong diurnal dependence of the near-surface temperature inversion. The magnitude of the temperature difference seems to be more consistent during the day than at night. These figures show that the PBL at the SGP site is

characterized by strong diurnal variation of temperature at the surface. The ground-based AERI sensor measures the surface temperature inversion that is largely missed by the satellite observations. A geostationary infrared sounder combined with ground-based infrared sounding would provide nearly continuous PBL monitoring.



**Figure 13. July 2019 SGP AERI uplooking (downwelling) BT from 675-680  $\text{cm}^{-1}$  (surface layer air T) (top panel) and 700-705  $\text{cm}^{-1}$  (elevated layer air T) shown in a boxplot analysis for each hour of the day (UTC hour). Same format as Figure 12.**



**Figure 14. July 2019 SGP AERI uplooking (downwelling) BT difference of surface minus elevated layer temperature shown in a boxplot analysis for each hour of the day (UTC hour). Same format as Figure 12.**

## Acknowledgments

Support is acknowledged from the NASA DSI program under grant 80NSSC22K1100.

Data were obtained from the Atmospheric Radiation Measurement (ARM) Program sponsored by the U.S. Department of Energy, Office of Science, Office of Biological and Environmental Research, Climate and Environmental Sciences Division.

## References

AIRS project (2019), Aqua/AIRS L2 Support Retrieval (AIRS-only) V7.0, Greenbelt, MD, USA, Goddard Earth Sciences Data and Information Services Center (GES DISC), Accessed: October 16, 2023, [10.5067/APJ6EEN0PD0Z](https://doi.org/10.5067/APJ6EEN0PD0Z).

Atmospheric Radiation Measurement (ARM) user facility. 2001. Balloon-Borne Sounding System (SONDEWNP). 2001-04-01 to 2023-04-11, Southern Great Plains (SGP) Central Facility, Lamont, OK (C1). Compiled by E. Keeler and K. Burk. ARM Data Center. Data set accessed 2023-04-12 at <http://dx.doi.org/10.5439/1595321>.

Atmospheric Radiation Measurement (ARM) user facility. 2004. Atmospheric Emitted Radiance Interferometer (AERISUMMARY). 2004-02-10 to 2023-04-10, Southern Great Plains (SGP) Central Facility, Lamont, OK (C1). Compiled by J. Gero, H. Revercomb, D. Turner, J. Taylor, R. Garcia, D. Hackel, B. Ermold and K. Gaustad. ARM Data Center. Data set accessed 2023-04-12 at <http://dx.doi.org/10.5439/1025146>.

Browell, E., S. Ismail, and W. Grant (1998), Differential Absorption Lidar (DIAL) measurements from air and space, *Applied Physics-B*, 67, 399-410.

Carroll, B. J., A. R. Nehrir, S. A. Kooi, J. E. Collins, R. A. Barton-Grimley, A. Notari, D. B. Harper, and J. Lee, 2022: Differential absorption lidar measurements of water vapor by the High Altitude Lidar Observatory (HALO): retrieval framework and first results. *Atmos. Meas. Tech.*, 15, 605-626, doi:10.5194/amt-15-605-2022.

Feltz, M. L., R. O. Knuteson, H. E. Revercomb, and D. C. Tobin (2014), A methodology for the validation of temperature profiles from hyperspectral infrared sounders using GPS radio occultation: Experience with AIRS and COSMIC, *J. Geophys. Res. Atmos.*, 119, doi:10.1002/2013JD020853.

Hair, J. W., et al. (2008), Airborne High Spectral Resolution Lidar for Profiling Aerosol Optical Properties, *Appl. Opt.*, 47, doi:10.1364/AO.47.006734.

Knuteson, R. O., F. A. Best, N. C. Ciganovich, R. G. Dedecker, T. P. Dirx, S. Ellington, W. F. Feltz, R. K. Garcia, R. A. Herbsleb, H. B. Howell, H. E. Revercomb, W. L. Smith, J. F. Short (2004a), Atmospheric Emitted Radiance Interferometer (AERI): Part I: Instrument design, *J. Atmos. Oceanic Technol.*, 21, 1763-1776.

Knuteson, R. O., F. A. Best, N. C. Ciganovich, R. G. Dedecker, T. P. Dirx, S. Ellington, W. F. Feltz, R. K. Garcia, R. A. Herbsleb, H. B. Howell, H. E. Revercomb, W. L. Smith, J. F. Short (2004b), Atmospheric Emitted Radiance Interferometer (AERI): Part II: Instrument performance, *J. Atmos. Oceanic Technol.*, 21, 1777-1789.

Loveless, D. M., T. J. Wagner, R. O. Knuteson, D. D. Turner, and S. A. Ackerman, 2022: Information Content of a Synergy of Ground-Based and Space-Based Infrared Sounders. Part I: Clear-Sky Environments. *J. Atmos. Oceanic Technol.*, 39, 771–787, <https://doi.org/10.1175/JTECH-D-21-0119.1>.

Loveless, D.M., et al., Combining the High Altitude Lidar Observatory (HALO) and Scanning High-Resolution Interferometer Sounder (S-HIS) for Thermodynamic Retrievals during the EcoDemonstrator Campaign, AMS Annual Meeting, 28 Jan–1 Feb 2024, Baltimore, MD.

Pagano, T. S., S. Broberg, H. H. Aumann, D. Elliott, E. Manning, and L. Strow, 2014: Performance status of the atmospheric infrared sounder ten years after launch. NASA JPL Rep., 9 pp., [https://trs.jpl.nasa.gov/bitstream/handle/2014/42928/12-5086\\_A1b.pdf](https://trs.jpl.nasa.gov/bitstream/handle/2014/42928/12-5086_A1b.pdf).

Rodgers, C. D., 2000: Inverse methods for atmospheric sounding: theory and practice (Vol. 2). World scientific.

ROM SAF, 2019: ROM SAF Radio Occultation Climate Data Record - COSMIC [Data set]. EUMETSAT SAF on Radio Occultation Meteorology, DOI:10.15770/EUM\_SAF\_GRM\_0003. [http://doi.org/10.15770/EUM\\_SAF\\_GRM\\_0003](http://doi.org/10.15770/EUM_SAF_GRM_0003)

Susskind, J., Barnet, C., & Blaisdell, J. (1998). Determination of atmospheric and surface parameters from simulated AIRS/AMSU/HSB sounding data: Retrieval and cloud clearing methodology. *Advances in Space Research*, 21(3), 369-384.

Tobin, D. C., et al. (2006), Radiometric and spectral validation of Atmospheric Infrared Sounder observations with the aircraft-based Scanning High-Resolution Interferometer Sounder, *J. Geophys. Res.*, 111, D09S02, doi:[10.1029/2005JD006094](https://doi.org/10.1029/2005JD006094).

Teixeira, João, et al. "Toward a global planetary boundary layer observing system: The NASA PBL incubation study team report." Toward a Global Planetary Boundary Layer Observing System: The NASA PBL Incubation Study Team Report (2021).

Turner, D. D., and U. Löhnert, 2021: Ground-based temperature and humidity profiling: Combining active and passive remote sensors. *Atmos. Meas. Tech.*, 14, 3033-3048, doi:10.5194/amt-14-3033-2021.

UCAR COSMIC Program, 2022: COSMIC-1 Data Products [Data set]. UCAR/NCAR - COSMIC, Access date: October 16, 2023, <https://doi.org/10.5065/ZD80-KD74>

UCAR COSMIC Program, 2019: COSMIC-2 Data Products [Data set]. UCAR/NCAR - COSMIC, Access date: October 16, 2023, <https://doi.org/10.5065/T353-C093>.